

Radar imaging of equatorial F region irregularities with maximum entropy interferometry

D. L. Hysell

Department of Physics and Astronomy, Clemson University, Clemson, South Carolina

Abstract. Radar interferometry with multiple collinear antenna baselines has been performed at Jicamarca, near Lima, Perú, and high-resolution images of plasma irregularities in equatorial spread F have been constructed from the data. The images represent the brightness distribution of the radar backscatter, which is the Fourier transform of the visibility or spatial cross correlation of the scattered radar signal on the ground. The visibility data are noisy and incompletely sampled, and we have used the maximum entropy method to perform the Fourier transform, making optimal use of the data available. Using the current antenna configuration at Jicamarca, the radar imaging technique is able to resolve structures within the radar beam that are just a few kilometers wide. By animating sequences of images, we can observe the evolution of ionospheric irregularities without confusing spatial and temporal variations.

Introduction

The postsunset equatorial F region ionosphere is frequently the site of plasma interchange instabilities, mechanisms which arise to release the free energy accumulated in the F region electron density profile throughout each day. The process by which the free energy is released is known as equatorial spread F . Spread F is a spectacular phenomenon often characterized by the rapid upward advection of field-aligned tubes of depleted electron density from the bottomside to the topside F region. Plasma waves with scale sizes between 11 cm and 1000 km have been observed. Outside the auroral zone, the most strongly driven dynamics in the ionosphere are found in the nighttime equatorial F region. (See reviews by *Woodman and La Hoz* [1976] and *Fejer and Kelley* [1980].)

Spread F has been studied for decades at the Jicamarca 50-MHz incoherent scatter radar located near Lima, Perú. Jicamarca observes intense nonthermal backscatter from 3-m irregularities embedded in the disturbed F region flow. These irregularities are thought to serve as tracers of the flow and therefore as telltales of large-scale ionospheric waves and insta-

bilities. In situ experiments carried out with instrumented sounding rockets have repeatedly confirmed that the regions of intense VHF radar backscatter are associated with deep electron density depletions. The Doppler velocities and interferometrically deduced drifts of the scattering regions typically agree, at least approximately, with plasma drifts deduced by other methods such as spaced-receiver scintillations and in situ electric field measurements.

Data from Jicamarca are typically presented in the form of range-time-intensity (RTI) plots of the kind shown in Figure 1. This figure shows backscatter power as a function of altitude and time during a bottomside spread F event. The height resolution is 1.5 km, and the time resolution is 6.4 s. The radar echoes between 250 and 300 km are consistent with so-called bottomside spread F , a commonly observed phenomena localized near altitudes where the F region density gradient is steepest. The feature above 300 km is a small example of a radar plume, which we associate with the upward advection of regions of low plasma density. Another very small plume can be seen at 2230 LT above 280 km.

The Doppler velocities measured in scattering layers such as these often match their range rates or apparent risings and fallings, as is the case for these layers. Furthermore, since the F region ionosphere can generally be thought to move eastward after sunset at 100–200 m/s, there is a widespread tendency

Copyright 1996 by the American Geophysical Union.

Paper number 96RS02334.
0048-6604/96/96RS-02334\$11.00

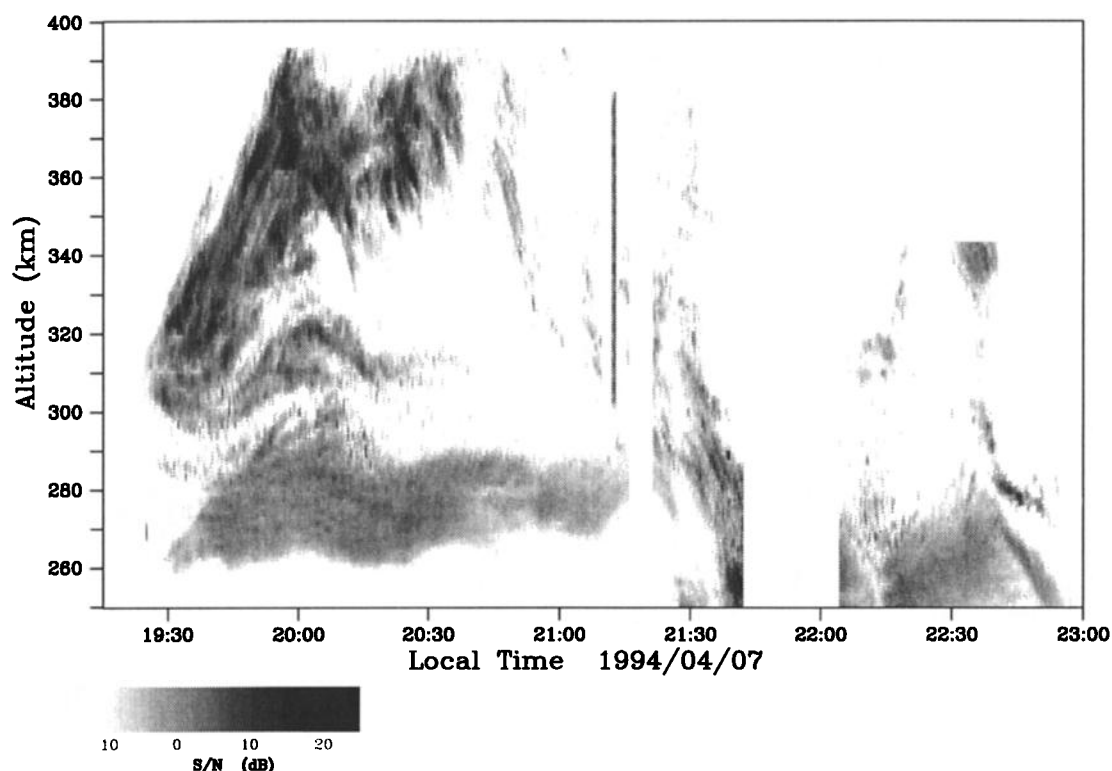


Figure 1. Range time intensity plot of a bottomside spread F event observed at Jicamarca. Gray scales represent the signal to noise ratio. The radar pulse repetition frequency (PRF) was 200 Hz, and the incoherent integration time is 6.4 s.

to interpret the temporal variations in the scattering structure as spatial variations in the zonal direction. One might then replace the time axis on Figure 1 with a spatial axis and view the plot as a picture of the disturbed F region ionosphere, to some approximation.

However, it is becoming clear that this is seldom a very good approximation. For one thing, the evolution timescale for the small- and intermediate-scale plasma irregularities seen by the radar may be short compared with the time they take to drift through the radar beam, let alone the hours it takes for a spread F event like the one in Figure 1 to unfold. Only very large scale features are in any sense frozen in to the flow. For another, the zonal drift speed of the F region ionosphere varies strongly with height below the F peak. We have estimated the zonal drift rate of the irregularities in Figure 1 interferometrically by the method of Kudeki *et al.* [1981]. While the irregularities at higher altitudes do drift eastward

at up to 150 m/s, many at lower altitudes seem to be drifting rapidly westward, and the height where the reversal takes place changes abruptly in time. Under these conditions, images like Figure 1 observed with the Jicamarca "slit camera" radar are likely to be very distorted representations. This is why steerable radars are the preferred instruments for studying the evolution of large-scale ionospheric structuring due to instabilities [see, for example, Tsunoda *et al.*, 1982].

Another problem with the conventional method of observing irregularities, even at Jicamarca, is that the spatial resolution is rather coarse. While the range resolution may be as fine as 150 m, the zonal resolution is limited by the antenna beam width. A 1° two-way beamwidth becomes 6 km wide at 350 km altitude. Because of the tremendous dynamic range of spread F echoes, irregularities many degrees out of the main antenna beam can be highly visible. Scattering structures with horizontal scale sizes less

than about 10–20 km are smeared beyond recognition in the RTI data by convolution with the antenna beam pattern and further smeared by time integration. Steering the radar cannot remedy the resolution problem and only exacerbates it.

Theoretical and empirical evidence suggest that there is interesting structure to be seen in bottom-side spread F with horizontal scale sizes of a few kilometers or less [Valladares *et al.*, 1983; Zargham and Seyler, 1987; Hysell, 1995]. If we wish to observe the structure with conventional radar techniques, we will need to build a steerable radar with a beam width much less than 1° .

A much more practical approach to the problem is to make the observations interferometrically using multiple antenna baselines. Rather than using a narrow, steerable antenna beam to observe small-scale targets in adjacent locations at sequential time intervals, interferometry sorts out precisely what structure is present within a broad radar beam in space and time independently. Increasing the resolution of an interferometer requires only lengthening and increasing the number of baselines, a cheap alternative to constructing larger main antenna arrays.

Using multiple spaced receivers for high-resolution remote sensing and imaging is commonplace in other fields like radio astronomy, seismology, active sonar, and medicine. Reviews of the principles involved are given by van Schooneveld [1979], Smith and Grandy [1985], and Thompson [1986], among many others. In the following section of the paper, we give a brief overview of the radar interferometry imaging problem as it applies to Jicamarca spread F observations and describe one method of high-resolution image reconstruction using maximum entropy. Following that, we give examples of radar images of intermediate-scale plasma irregularities concealed in the RTI plot in Figure 1. Finally, we discuss the implications of the images on our understanding of spread F and indicate the direction of future research.

Radar Interferometry

Radar interferometry was introduced by Woodman [1971] and further developed by Farley *et al.* [1981] and Kudeki *et al.* [1981] for irregularity studies at Jicamarca. Although the basic technique has found other applications, particularly in the mesosphere-stratosphere-troposphere (MST) radar field where it has been expanded upon considerably, only recently

has much attention been given to updating the technique for ionospheric work. (The literature surrounding MST radar wind profiling with interferometry is extensive. Interested readers can consult Doviak *et al.* [1994] for a review of the subject.) The basic idea is that by correlating the radar signals received on spatially separated antennas, one can deduce the moments of the arrival-angle distribution of the backscatter and so investigate the structure of the scattering medium in the direction transverse to the radar beam. Interferometry often has practical advantages over beam-steering approaches, narrow interferometry sidelobes usually being easier to arrange than a narrow antenna main beam.

If we view the backscatter as a spectrum of incoming plane waves, then the signal present at the output of a coherent radar receiver can be written as

$$V(t) = \int d\Omega d\omega E(\sigma, \omega) \mathcal{A}(\sigma) e^{i(\mathbf{k} \cdot \mathbf{x} - \omega t)} \quad (1)$$

where ω refers to the baseband frequency, σ is a unit vector in the direction of the wave vector \mathbf{k} , E is the spectrum of wave amplitudes, \mathcal{A} is the receiving antenna array factor, and the integration is over solid angle elements in the sky $d\Omega$. The product of the signals from spatially separated antennas is then

$$\begin{aligned} V_1^* V_2 &= \int d\Omega d\Omega' d\omega d\omega' E^*(\sigma, \omega) E(\sigma', \omega') \\ &\cdot \mathcal{A}^*(\sigma) \mathcal{A}(\sigma') e^{-i(\mathbf{k} \cdot \mathbf{x}_1 - \omega t)} e^{i(\mathbf{k}' \cdot \mathbf{x}_2 - \omega' t)} \quad (2) \end{aligned}$$

In accordance with the central limit theorem, the scattering is a random process, the scatter is incoherent, and the amplitudes of individual components of the plane wave spectrum are Gaussian random variables. It is only upon ensemble average that the cross correlation in (2) is a well-defined quantity. Since the amplitudes of waves scattered from different arrival angles and frequencies are uncorrelated,

$$\begin{aligned} \langle E^*(\sigma, \omega) E(\sigma', \omega') \rangle \\ = \langle |\tilde{E}(\sigma, \omega)|^2 \rangle \delta(\sigma - \sigma') \delta(\omega - \omega') \end{aligned}$$

the cross-correlation function formed by averaging (2) becomes

$$\langle V_1^* V_2 \rangle = \int d\Omega d\omega \langle |\tilde{E}(\sigma, \omega)|^2 \rangle |\mathcal{A}(\sigma)|^2 e^{i\mathbf{k} \cdot \mathbf{d}_{12}} \quad (3)$$

or symbolically

$$g(k\mathbf{d}) = \int d\Omega d\omega f(\sigma, \omega) \mathcal{A}(\sigma) e^{i\mathbf{k} \cdot \mathbf{d}\psi} \quad (4)$$

where g is the covariance or spatial cross-correlation function of the antenna separation vector \mathbf{d}_{12} , f is the power density spectrum of the backscatter as a function of arrival angle and Doppler frequency, A is the normalized antenna gain factor, and ψ is the direction cosine between \mathbf{k} and \mathbf{d} . In the language of radio astronomy, g is the observed visibility spectrum and f is the sought-after brightness distribution. Note that we could equally well compute the visibility distribution in the frequency domain, in which case the integral over Doppler frequency would not appear. In practice, the ensemble average implied in the angle brackets in the calculation is replaced by a time average, with resulting statistical errors and stationarity restrictions.

Single-Baseline Interferometry

Conventional interferometry experiments for ionospheric work make use of a single separation baseline along with (4) to determine the first three moments of the brightness spectrum. By normalizing (4) to the total backscattered power P , recognizing that the brightness plays the role of a distribution function, and expanding in a power series about $\langle\psi\rangle$, we have

$$\begin{aligned} P &= \int d\Omega d\omega f(\sigma, \omega) A(\sigma) \\ g(kd) &= P \langle e^{ikd\psi} \rangle \\ g(kd) &= P e^{ikd\langle\psi\rangle} \left(1 - \frac{1}{2} k^2 d^2 (\langle\psi^2\rangle - \langle\psi\rangle^2) + \dots \right) \end{aligned} \quad (5)$$

which gives the mean arrival angle and rms width of the scattering distribution with respect to the interferometry baseline. In ionospheric work, the irregularities are strongly field aligned, and the radar backscatter is confined to the plane perpendicular to \mathbf{B} ; the problem is therefore two-dimensional, and ψ alone is sufficient to specify the position of scattering structures at a given range so long as the baseline has a finite component perpendicular to \mathbf{B} . The cross-correlation function in (5) can be computed in the time or frequency domain and is often used to estimate plasma irregularity drift rates given by the time rate of change of $\langle\psi\rangle$. Note that unlike in MST interferometry work, we do not involve the Doppler frequency in the drift rate estimate. This is because the phase velocities of ionospheric plasma irregularities are not generally taken to be representative of the bulk flow of the medium.

Imaging the Brightness Spectrum

It is obvious that with more receivers and more interferometry baselines, the basic interferometry technique can offer additional information about the arrival angle distribution of the radar backscatter. In the case of equatorial ionospheric plasma irregularities, we would like to invert (4) and estimate the brightness distribution in the equatorial plane. Computed for each Doppler frequency, this distribution is literally the most complete description of what is taking place within the scattering volume that we could hope for. If we rewrite (4) in terms of the direction cosine ψ and assume that ψ is small, it becomes clear that the visibility spectrum on the ground and the brightness distribution are Fourier transform pairs. (This is a well-known result that appears in many remote sensing contexts.)

$$\begin{aligned} g(kd, \omega) &= \int \frac{d\psi}{\sqrt{1-\psi^2}} f(\psi, \omega) A(\psi) e^{ikd\psi} \\ &\Rightarrow f(\psi, \omega) A(\psi) \end{aligned} \quad (6)$$

where d is the zonal distance between spaced receivers and ψ is approximately equal to the zenith angle in the plane perpendicular to \mathbf{B} .

One could then make visibility measurements with a large number of collinear, spaced antennas having baselines that are integer multiples of some fundamental length d_0 . By the sampling theorem, these measurements would be sufficient to completely recover the brightness spectrum provided that it was band limited within a range of λ/d_0 radians. (This condition can be guaranteed with the right choice of transmitter beam width.) Since only a finite number of visibility measurements can be made in practice, windowing of the visibility spectrum will generally be necessary to suppress spectral artifacts. A price has to be paid, in the form of reduced resolution in the resulting brightness spectrum. Nevertheless, the measurements can be made, and the brightness can be computed with windowed discrete Fourier transforms. *Kudeki and Sürücü* [1991] and *Sürücü and Kudeki* [1992] have performed the experiment just described at Jicamarca and presented brightness spectra from the equatorial electrojet and a bottomside spread F layer. Their results confirmed that there is much to be learned about the structure of the unstable ionosphere by going beyond the simple analysis leading to (5).

The longest interferometry baseline currently available at Jicamarca is approximately 356 m, 7 times the length of the shortest available, and about 59 wavelengths long. Yet we know that the correlation length of spread F echoes on the ground can be much longer than this; signals received on the most widely separated antennas at Jicamarca are sometimes almost perfectly correlated! Furthermore, with only four receivers available at Jicamarca, it is impossible to measure the visibility at the longest separation distance without leaving gaps in the discrete visibility spectrum. The visibility data available are therefore necessarily incomplete. Spectral windowing is one way to manage the problem, but it essentially requires you to ignore much of the hard-fought interferometry data collected at large spatial separations. In the case of bottomside spread F , there is strong evidence suggesting that an important class of waves could be seen by Jicamarca if the brightness distributions could be resolved perhaps a few times more finely than they have been so far.

We have tried to make the most of new, unavoidably incomplete visibility data from Jicamarca by implementing the maximum entropy method (MaxEnt). This approach to inverting (6) is familiar to the radio astronomy community which has refined and implemented it routinely for about two decades. It attempts to answer the question, What is the most reasonable, least prejudicial brightness distribution consistent with whatever noisy, incomplete visibility data are available? This technique should not be confused with the more familiar one of the same name for general spectral estimation, although the two are distantly related. In fact, the terms "maximum entropy" and "maximum likelihood" are applied to a number of different methods and philosophies for inferring unmeasured quantities on the basis of some overarching principle. The maximum entropy method algorithm we have adopted is briefly described in the next section of the paper after a short introduction.

Maximum Entropy Method

High-resolution spectral methods make inferences regarding unmeasured data other than that they are zero or periodic continuations of measured data. Some sort of model is therefore necessary, and a number of models are in common use. The CLEAN algorithm, for instance, models the brightness distribu-

tion as a collection of point sources whose patterns have been convolved with the interferometer lobe pattern. Deconvolution is carried out by a process of subtracting distorted point sources from a trial brightness distribution, or "map" (computed from the visibility with a DFT), while adding corresponding undistorted point sources to another "clean" map. The process is repeated until the original "dirty" map is in some sense empty, at which point the clean map should be the desired image. In contrast, predictive spectral algorithms model the raw data as the output of an autoregressive (AR) process of some order driven by white noise and represent the spectrum of the data, which is the brightness in our case, with an all-poles model. Such a model can provide an accurate facsimile of spectra with multiple, sharp peaks. Model coefficients can be calculated either from the covariance of the data or from the data directly through a process involving mean-square error reduction.

However, both of these approaches have a certain ad hoc quality. In the case of CLEAN, the choice of the loop gain (the amplitude of the point source removed from the dirty map each time) is crucial and yet subjective, and the method seems generally unable to reproduce test maps with broad features in any case. As for the AR method, there may be no way to know a priori what the order of the process is, leaving open the possibility that the method may produce more or fewer spectral peaks than truly exist.

We focus our attention instead on the maximum entropy method (MaxEnt) which is motivated by the following "first principle of data reduction" stated by *Ables* [1974, p. 383]: "The result of any transformation imposed on the experimental data shall incorporate and be consistent with all relevant data and be maximally non-committal with regard to unavailable data." The transformation from the visibility to the brightness spectrum that adheres to this philosophy is the one which maximizes the "entropy" of the map in the information and communication theory sense of the word. *Shannon and Weaver* [1949] defined entropy as a measure of the uncertainty associated with a probability distribution function; the greater the entropy of a proposition, the greater the number of questions that must be asked to ascertain if the proposition is true. Choosing a proposition or a map with less than the maximum entropy implies knowledge that had better be possessed by data analysts

wishing to avoid bias. Jaynes' principle then says that maximizing the entropy of the map while maintaining consistency with the measurements is the way to obey Ables' principle.

It has since been recognized in problems such as ours, where the map is positive definite, that the entropy expression can be interpreted as the multiplicity of ways that the map could be constructed. Of all of the maps which are consistent with the visibility data, the one with the highest entropy is the one with the greatest multiplicity of realizations, the one most representative of the class of all possible solutions, and the one most likely to have occurred. This multiplicity represents the prior probability of a map, which can be incorporated into the Fourier transform inversion problem using Bayesian statistics. Bayesian statistics offer a method of including preferences for certain solutions in statistical inference. We do not make explicit use of Bayesian probability calculus in this paper but arrive at the same formulas as if we had.

Suppose the brightness distribution is composed of n discrete zenith angle bins. Into each i th bin, a discrete number f_i of radiation quanta fall indistinguishably such that the total number of quanta in the distribution sum to $\sum_{i=1}^n f_i = F$. Then the number of ways a particular given map can be realized is $F!/\prod_{i=1}^n f_i!$. Assuming that the quanta fall into the different bins with equal probability, the most likely map to result from a random placement of quanta is the one for which this ratio is highest. With the application of Stirling's formula and the assumption that the quanta are numerous, it can easily be shown that maximizing this ratio is tantamount to maximizing the quantity $S = -\sum_{i=1}^n f_i \log f_i / F$, which is the configurational entropy of the distribution. Given no other prior information, the distribution with the highest entropy is the most likely one. (This result is the basis upon which partition functions in statistical mechanics are derived.)

In the case of interferometric imaging, the map with the highest entropy is the one least committal to unmeasured data. Not only is it the most likely brightness spectrum, but also it is one near which most other possible spectra are concentrated in solution space. To choose a spectrum with lower entropy would be to ignore the majority of possible outcomes of the inversion problem and focus on a less likely subclass of solutions, an unwarranted step to the extent other prior information is unavailable. A

thorough and compelling discussion of the rationale for the MaxEnt along these lines has been given by Jaynes [1982]. Other good reviews of the MaxEnt principle have been given by Jaynes [1985], Daniell [1991], and Skilling [1991].

The problem then is to find the map with the greatest entropy ($S = -\int d\psi f(\psi) \ln f(\psi) / F$ being the continuous version) consistent with whatever data are available to the accuracy with which they are known, a constrained maximization problem. Since the map must be one for which the entropy is calculable, the expression for entropy serves as a regularizing function. MaxEnt maps necessarily possesses the desirable properties of being positive and in some sense the smoothest distributions allowed by the data. The maximum entropy method therefore infers the values of unmeasured data so as to guarantee a positive map while rejecting sidelobes and other spurious features not pointed to by measurements.

In fact, the form of the entropy given above, sometimes called Shannon entropy, or H2, is only one of the possible regularizing functions that might be used. Another form of entropy sometimes used is $S = \int d\psi \ln \psi$, called H1. Other choices of regularizing functions that impose positiveness, smoothness, and uniformity are possible. Press *et al.* [1988] even argue that regularization of the map is the key to the success of the MaxEnt rather than the concentration theorem and that MaxEnt is perhaps no better or worse than other regularizing schemes without foundations in information theory. The apparent interchangeability of H1 and H2 in practice and the failure of MaxEnt to function in the presence of a background noise bias lend credence to this point of view, at least for the case of small data sets, but we nonetheless adopt H2 as the regularizing function in an attempt to adhere to Jaynes' principle.

Cornwell and Evans [1985] also take issue with the information theory interpretation of maximum entropy, arguing that nothing in the radio imaging problem aptly plays the role of a probability distribution function. For them, the purpose of MaxEnt is to construct an image that is as close to some prescribed target image as allowed by the data. Entropy to them is just a metric for measuring how close the solution is to the target. But in our radar imaging application, we have no preconceived target image in mind other than that it should be nonnegative. It may eventually prove advantageous to utilize maps produced by windowed spectral analysis or CLEAN

either as target images or as further prior information for defining the configurational entropy. These possibilities are left for future investigation.

MaxEnt Algorithm

Let g_j be either the real or imaginary component of the measured spatial cross-correlation function for some separation distance. The number of such independent data points N is equal to twice the number of nonredundant interferometry baselines plus 1 (for the zero lag $g(0)$). The set of all $j=1 \dots N$ such values constitute the radar interferometry data for one range gate and one integration period. Each g_j was measured with a baseline of length d_j , and with each measurement is associated a statistical error e_j . Then the Fourier transform relationship between the visibility and brightness spectra gives

$$g_j + e_j = \int d\psi f(\psi) \cos/\sin(kd_j\psi) \quad (7)$$

$$g_j + e_j = \int d\psi f(\psi) h_j(\psi) \quad (8)$$

where $h_j(\psi)$, the point-spread function of the interferometer, is either the cosine or sine of multiples of the zenith angle depending on whether g_j is the real or imaginary part.

For the brightness distribution, or "map" $f(\psi)$, we adopt the following form:

$$f(\psi) = Z^{-1} F e^{-\sum_j \lambda_j h_j(\psi)} \quad (9)$$

$$Z = \int d\psi e^{-\sum_j \lambda_j h_j(\psi)} \quad (10)$$

where F is the total integrated brightness and the normalization term Z is like the Gibbs canonical partition function from statistical mechanics. The motivation for writing the brightness this way comes from maximizing the expression for H2 constrained by (7), where one constraint for each data point enters with a Lagrange multiplier λ_j . Solving for the brightness distribution gives an expression of the form of (9), which we can show by working backward and writing the entropy H2 in terms of $f(\psi)$ above.

$$S(f) = \sum_j \lambda_j (g_j + e_j) + F \ln Z + \Lambda \left(\sum_j e_j^2 / \sigma_j^2 - \Sigma \right) \quad (11)$$

The first line of (11) is an exact relation between the entropy of the map, the partition function, and the weighted data points. This expression will be maximized as if a problem in variational mechanics, and in that spirit, a final constraint on the norm of the statistical error terms has been introduced with one more Lagrange multiplier Λ (this is essentially the χ^2 method of *Wilczek and Drapatz* [1985] for introducing statistical noise into the MaxEnt problem, generalized here for complex data). Without allowances for noise in the data, MaxEnt would tend to dismiss high-entropy subclasses of solutions, painstakingly reproducing spectral artifacts consistent with the statistical errors. The MaxEnt technique becomes appropriate for noisy data only when it is allowed to migrate away from the measured visibility in a constrained way in search of a map with greater entropy. As MaxEnt climbs uphill in entropy as far as the σ_j^2 allow, the algorithm recognizes statistical fluctuations for what they are and smoothes the map so as not to generate artifacts. The expected variances of the visibility estimates are known functions of the signal-to-noise ratio, the number of statistically independent samples, and the coherence. With the assumption that the statistical fluctuations are normal, uncorrelated, zero-mean random variables so that the error terms are χ^2 , we can set Σ equal to the number of data points as an approximation and proceed with the solution. (See *Andrews and Hunt* [1977] and *Press et al.* [1988] for further discussions of the ill-behaved nature of the MaxEnt problem which ignores noise.)

Differentiating $S(f)$ with respect to λ_j gives the relationship between the measurements, errors, and the brightness distribution:

$$\frac{\partial S}{\partial \lambda_j} = 0 = g_j + e_j - F \langle h_j \rangle \quad (12)$$

where the angle brackets denote an average over the brightness distribution function (9). Differentiating with respect to the error terms e_j relates those terms to the Lagrange multipliers.

$$\frac{\partial S}{\partial e_j} = 0 = \lambda_j + \frac{2\Lambda}{\sigma_j^2} e_j \quad (13)$$

Finally, the error constraint allows us to solve for Λ in terms of the other quantities.

$$\frac{\partial S}{\partial \Lambda} = 0 \rightarrow \Lambda^2 = \sum_j \frac{\lambda_j^2 \sigma_j^2}{4\Sigma} \quad (14)$$

Taken together, (9), (12), (13), and (14) form a well-posed system of N simultaneous nonlinear equations for N Lagrange multipliers that can be solved numerically. Averaging over the brightness spectrum can be done discretely, although care has to be taken to avoid line-splitting artifacts [Jaynes, 1982]. We have had good success solving these equations for real and test data using a newton method, computing the Jacobian matrix by finite differences. The algorithm is quite stable and is not particularly sensitive to initial conditions. (Like Wilczek and Drapatz [1985], we initialize the λ_j with small values consistent with a flat map.) Other, faster numerical solvers have also shown promise with these equations.

There are several other approaches to the maximum entropy problem available in the literature. (Skilling and Bryan [1984], for instance, developed a general algorithm capable of handling a very large number of data points.) Whereas we have discussed a direct solution technique above, some techniques iterate the map itself toward a maximum entropy configuration [see, for example, Gull and Daniell, 1978; Wu, 1984; Cornwell and Evans, 1985]. We have implemented the second-order Wu [1984] algorithm and found that it converges to the same maps as the one described above, albeit more slowly for the number of data points ($N=13$) tried. A gnawing problem inherent in the iterative technique is a certain amount of uncertainty regarding how long one should iterate. How much does one weigh the desire for maximum entropy against the desire to meet the constraints? The same problem is inherent in the direct solver technique outlined above and lurks in the choice of the parameter Σ , which is only known approximately. The exact choice does not seem to be important in our high signal-to-noise-ratio application, however.

Skilling [1991] discusses this problem of weights and also points out further generalizations of MaxEnt. For one thing, the expression for the configurational entropy can be modified to take into account preferences for some bins over others. Ideally, the entropy formula should make allowances for the radar antenna array factor, although we have yet to take this into account. For another, MaxEnt tacitly assumes that the pixels in the brightness map are uncorrelated. In fact, neighboring pixels in any reasonable image are usually correlated, and if one sets out to ignore this, one may produce images with spurious bright spots. In the future, we will evaluate the benefits of generalizing MaxEnt in these two ways as far as ionospheric radar imaging goes.

Observations

Figure 2 shows the configuration of the Jicamarca antenna array during the April 7, 1994, spread F observations. The north and south array quarters were used for transmission, and four independent modules (64ths) were used for reception. The east-west spacings between antennas are multiples of $d_0 \approx 50.9$ m. With the given configuration, baseline lengths between $(0 \cdots 7) \times d_0$, excluding $3 \times d_0$, were available for the measurement of the spatial cross-correlation function of the radar scatter on the ground. The minimum baseline length is sufficiently short so long as the scatter is confined to an angular spread no more than 6.75° wide. An advantage of radar imaging over radio astronomy is that we can control the width of the scattering brightness distribution by controlling the beam width of the transmitting antenna which illuminates the scattering volume. Figure 3 shows the normalized computed power pattern of the Jicamarca antenna, as configured for transmission, at the locus of perpendicularity to \mathbf{B} at an altitude of 400 km. The half power full beam width is approximately 2° , and the radiated power is reduced by 30 dB out-

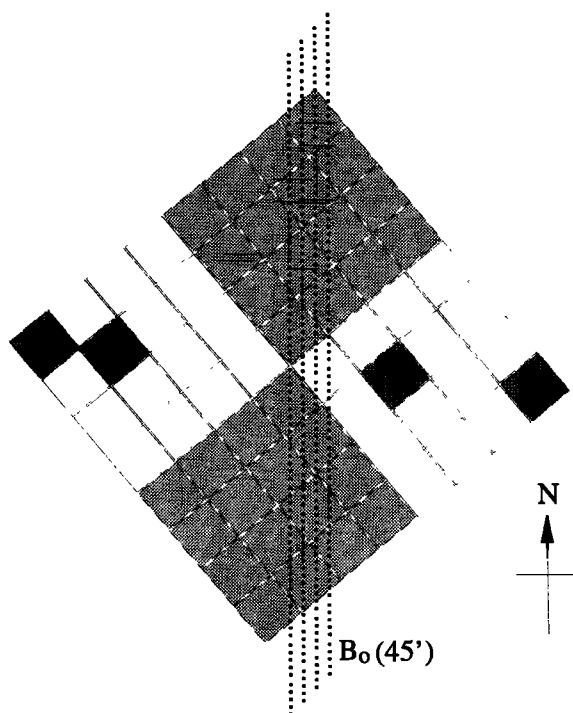


Figure 2. Diagram of the connections to the Jicamarca main antenna array. The north and south quarters were used from transmission, and four modules were used for reception.

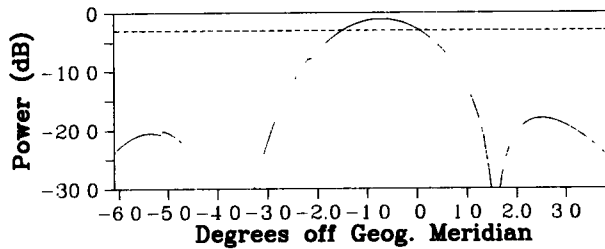


Figure 3. One-way antenna beam pattern for the north and south quarters of the Jicamarca antenna, traced along the locus of perpendicularity at an altitude of 400 km.

side of a 6.75° full width. We do not bother to divide out the transmitter antenna power pattern from our computed maps, in part because the physical features of interest to us are significantly narrower than the antenna beam width and in part because the curve in Figure 3 is only an idealization. Furthermore, it is clear that some of the features that emerge in the maps are aliased after all, complicating their proper normalization. The receiving antenna beam widths are much broader than the transmitting power pattern, and we neglect them entirely.

The expected variance of the individual components of the visibility spectrum can be estimated precisely with the help of the error estimator expressions given by *Farley and Hysell* [1996]. For the time being, we have been more casual and have assigned a uniform variance consistent with a high signal-to-noise ratio, moderate coherence, and the number of incoherent integrations of each visibility component. We have also ignored the fact that the statistical errors between lags are correlated. A more precise treatment of the problem will follow in later generations of the data processing program.

The visibility spectra can be computed in the frequency domain, allowing us to produce image maps for each Doppler frequency. It should ultimately prove interesting to contrast maps corresponding to different Doppler frequencies. The data presented here have been sorted into four Doppler bands, with the zero-frequency component containing most of the power. Maps of this component will be shown. In fact, maps corresponding to all four Doppler frequencies seem to resemble one another fairly closely in this instance.

Subtraction of the background noise turns out to be a crucial step in our imaging process. Perhaps

more than any other factor, the constraint that the brightness distribution be positive discourages the MaxEnt algorithm from reproducing spectral artifacts due to unsampled and noisy data. A significant background noise floor in the data dilutes the impact of this constraint and, in some cases, permits the MaxEnt spectrum to revert to the DFT of the incomplete data. Unfortunately, noise gates were not sampled during this particular radar experiment. Noise has instead been estimated on the basis of data from a Doppler bin with very little signal power using the method of *Hildebrand and Sekhon* [1974]. It is of course important to subtract the noise bias from the zero lag of the visibility as well as from the terms used to normalize the other lags and to use the same samples for normalization as for the cross correlation.

We illustrate the effectiveness of the maximum entropy image reconstruction technique with two examples taken from the bottomside spread F data. The first example is Figure 4, which depicts the passage of a mini radar plume over the radar late in the evening. In these figures, the vertical axis is altitude, the horizontal axis is zenith angle (from

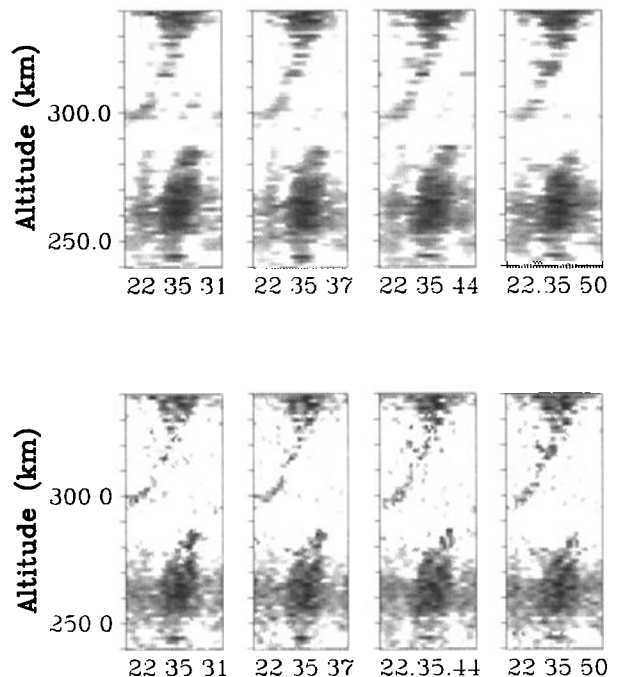


Figure 4. Radar imaging data, plotted against altitude and zenith angle. The upper panels show the results of lag window spectral analysis, and the lower panels show MaxEnt results.

$\pm 3.38^\circ$), and the gray scales represent signal-to-noise ratios from -3 to 27 dB. Each row is composed of 32 pixels. The incoherent integration time from frame to frame is 6.4 s. Most of the scattered power comes from near zenith, but a significant amount evidently arrives from outside the transmitting antenna half-power beam width. This is no surprise, given the dynamic range of the target. Features in the mini-plume become clearer as they slowly drift over the center of the radar from left to right, east to west. The mini-plume ultimately vanishes after several more frames as it drifts ever eastward at about 150 m/s.

The upper panels show images computed with windowed fast Fourier transforms (FFTs) of the visibility data, and the lower ones show the same data processed with the MaxEnt algorithm. While the same overall trends can be found in both sets of images, MaxEnt has clearly been able to resolve fine structure down to the single pixel level otherwise lost. We see, for instance, that the mini-plume is a narrow channel not more than 1 km wide at some points and that it may have bifurcated at 320 km altitude. Although the bottomside layer between 250 and 275 km appears diffuse and undifferentiated in the upper panels, the lower panels reveal periodic, vertically elongated structures at the layer surface, propagating eastward and shearing. We also find several localized, enduring "hot spots" in the MaxEnt images that may signify backscatter from particularly steep plasma density gradients in the unstable medium.

Figure 5 is another example of what we can achieve with MaxEnt radar imaging. These images come from earlier in the evening when there were multiple bottomside scattering layers. They are plotted in the same way as the previous set of figures except that the gray scales now represent signal-to-noise ratios of 5–35 db. The MaxEnt images give a clear impression of multiple diagonal lines intersecting the transmitting radar beam above about 300 km. These lines, which run from lower left to upper right, are separated by about 5–10 km and bear some resemblance to computer simulations of the quasi-normal modes of the intermediate-scale collisional interchange instability *Zargham and Seyler, 1987*. A few examples of localized scattering hot spots are also visible. It is these hot spots that are mainly tracked by the normal interferometric drifts technique.

Some aspects of the images just described are admittedly much easier to perceive when the images

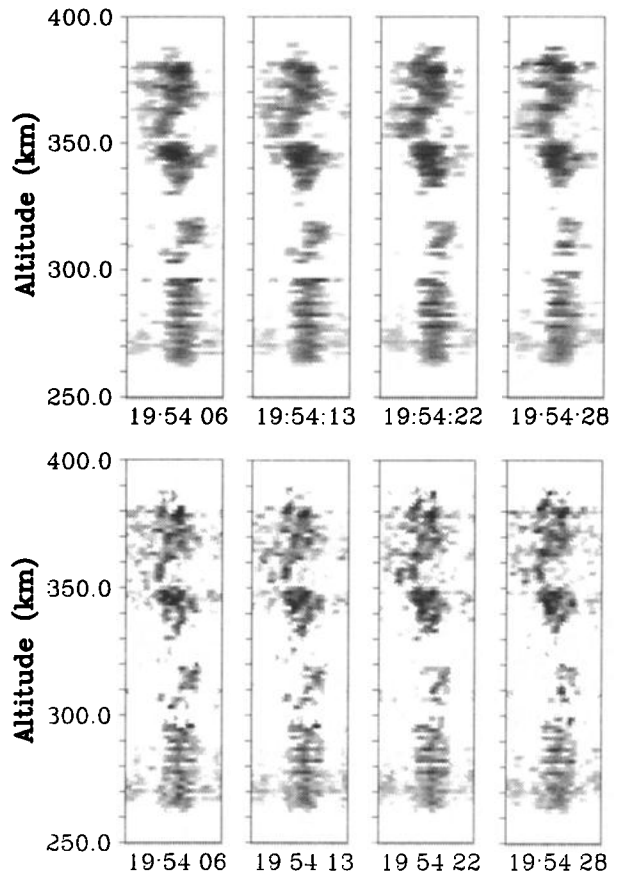


Figure 5. Same as Figure 4, except for an earlier time.

are animated. The overall consistency of the brightness maps, from range to range and time to time, and the absence in the maps of most of the spectral artifacts that arise in unwindowed FFTs of the visibility suggest that the MaxEnt algorithm is performing as well in this application as it has in many others. The algorithm has also been shown to work admirably with a variety of test data. The criteria for judgment are that the algorithm should suppress artifacts in the map due to noisy and incompletely sampled data without introducing any additional, unwarranted features.

Conclusions and Future Work

Until now, VHF coherent backscatter radars were best suited for studying the microphysics of ionospheric plasma instabilities at the Bragg scattering wavelength and, to some extent, the large-scale struc-

ture and dynamics as captured in RTI diagrams. By dramatically improving the cross-beam spatial resolution and differentiating between temporal and spatial variations in the scattering medium, interferometric imaging opens a new area of study at Jicamarca and other radar facilities with interferometric capability. In this particular case, we have been able to observe the growth and evolution of intermediate-scale gradient drift and interchange instabilities in the equatorial ionosphere directly.

In the equatorial electrojet and bottomside spread F , the physical scale size of most interest is approximately 1 km (corresponding to the wavelength of the fastest growing gradient drift and interchange instability normal modes). In order to resolve kilometer-scale features at F region heights, we must make use of high-resolution spectral techniques such as MaxEnt, which utilizes the available, noisy data in an optimal way and makes reasonable inferences regarding unknowns. To increase the resolution of the technique still further at Jicamarca, an additional antenna module for interferometry is being constructed west of the main array. The new module will approximately double the maximum baseline length available. We envision performing experiments with 6 receivers and 15 nonredundant baselines, spanning lengths from half the shortest to twice the longest baselines used in the current experiments. In addition to increasing the resolution and field of view of the imaging technique, more baselines afford us the opportunity to verify the efficacy of the MaxEnt. We could, for instance, compute MaxEnt maps with a subset of the baselines and compare the results with DFT maps made from all available data.

High-resolution imaging facilitates for the first time careful comparisons between experiment and computer simulations of gradient drift and interchange instabilities. While there is always some uncertainty about the validity of these codes at large scales (because of mesh size limitations, nonlocal effects parallel to the magnetic field, etc.), the intermediate scale simulations are much simpler and therefore more reliable. In addition to comparing the morphology of the radar images with simulations, we could calculate the plasma flow field from sequential radar images (using methods discussed by Schalkoff [1989] perhaps) and compare the results with simulations of irregularity streamlines. This could be a definitive way to determine the altitude where the F region makes a transition from laminar to turbulent flow.

Finally, one of the most compelling reasons to study equatorial ionospheric irregularities in the first place is that they often generate intense radio scintillation storms. Since the first Fresnel zone for VHF scintillations is approximately 1 km at F region heights, we can investigate the ionospheric phase screen responsible for scintillations by imaging kilometer scale waves near the F peak. Efforts will be made to coordinate interferometry experiments at Jicamarca with the overhead passage of radio sources and to correlate measured scintillation spectra with the radar images.

Acknowledgments. The author gratefully acknowledges helpful input from E. Kudeki and J. D. Sahr. This work was supported by the National Science Foundation through cooperative agreements ATM-9022717 and ATM-9408441 and by NSF grants ATM-9415931 and ATM-9424550. The Jicamarca Radio Observatory is operated by the Geophysical Institute of Perú, Ministry of Education, with support from the NSF Cooperative Agreements just mentioned. The help of the staff, especially Ronald Woodman, was much appreciated.

References

- Ables, J. G., Maximum entropy spectral analysis, *Astron. Astrophys. Suppl. Ser.*, **15**, 383, 1974.
- Andrews, H. C., and B. R. Hunt, *Digital Image Restoration*, Prentice-Hall, Englewood Cliffs, N. J., 1977.
- Cornwell, T. J., and K. F. Evans, A simple maximum entropy deconvolution algorithm, *Astron. Astrophys.*, **143**, 77, 1985.
- Daniell, G. J., Of maps and monkeys, in *Maximum Entropy in Action*, edited by B. Buck, and V. A. Macaulay, chap. 1, pp. 1–18, Clarendon, Oxford, 1991.
- Doviak, R. J., R. J. Latatis, C. L. Holloway, and J. Van Baelen, A generalized theoretical analysis of cross-correlation and cross-spectra for spaced antenna wind profilers, *Tech. Rep. TN-407*, Nat. Cent. for Atmos. Res., Boulder, Colo., 1994.
- Farley, D. T., and D. L. Hysell, Radar measurements of very small aspect angles in the equatorial ionosphere, *J. Geophys. Res.*, **101**, 5177, 1996.
- Farley, D. T., H. M. Ierkeic, and B. G. Fejer, Radar interferometry: A new technique for studying plasma turbulence in the ionosphere, *J. Geophys. Res.*, **86**, 1467, 1981.

- Fejer, B. G., and M. C. Kelley, Ionospheric irregularities, *Rev. Geophys.*, **18**, 401, 1980.
- Gull, S. F., and G. J. Daniell, Image reconstruction from incomplete and noisy data, *Nature*, **272**, 686, 1978.
- Hildebrand, P. H., and R. S. Sekhon, Objective determination of the noise level in Doppler spectra, *J. Appl. Meteorol.*, **13**, 808, 1974.
- Hysell, D. L., The decay of equatorial *F* region plasma depletions, paper presented at the IUGG XXI General Assembly, Boulder, Colo., July 2–14, 1995.
- Jaynes, E. T., On the rationale of maximum-entropy methods, *Proc. IEEE*, **70**, 939, 1982.
- Jaynes, E. T., Where do we go from here?, in *Maximum-Entropy and Bayesian Methods in Inverse Problems*, edited by C. R. Smith, and W. T. Grandy Jr., chap. 2, pp. 21–58, D. Reidel, Norwell, Mass., 1985.
- Kudeki, E., B. G. Fejer, D. T. Farley, and H. M. Ierick, Interferometer studies of equatorial *F* region irregularities and drifts, *Geophys. Res. Lett.*, **8**, 377, 1981.
- Kudeki, E., and F. Sürücü, Radar interferometric imaging of field-aligned plasma irregularities in the equatorial electrojet, *Geophys. Res. Lett.*, **18**, 41, 1991.
- Press, W. H., B. P. Flannery, S. A. Teukolsky, and W. T. Vetterling, *Numerical Recipes in C*, Cambridge Univ. Press, New York, 1988.
- Schalkoff, R. J., *Digital Image Processing and Computer Vision*, John Wiley, New York, 1989.
- Shannon, C. E., and W. Weaver, *The Mathematical Theory of Communication*, Univ. of Ill. Press, Urbana, 1949.
- Skilling, J., Fundamentals of MaxEnt in data analysis, in *Maximum Entropy in Action*, edited by B. Buck, and V. A. Macaulay, chap. 2, pp. 19–40, Clarendon, Oxford, 1991.
- Skilling, J., and R. K. Bryan, Maximum entropy image reconstruction: General algorithm, *Mon. Not. R. Astron. Soc.*, **211**, 111, 1984.
- Smith, C. R., and W. T. Grandy Jr. (Ed.), *Maximum-Entropy and Bayesian Methods in Inverse Problems*, D. Reidel, Norwell, Mass., 1985.
- Sürücü, F., and E. Kudeki, Radar imaging studies of bottomside equatorial spread *F*, paper presented at Coupling, Energetics, and Dynamics of Atmospheric Regions meeting, Boulder, Colo., June, 1992.
- Thompson, A. R., *Interferometry and Synthesis in Radio Astronomy*, John Wiley, New York, 1986.
- Tsunoda, R. T., R. C. Livingston, J. P. McClure, and W. B. Hanson, Equatorial plasma bubbles: Vertically elongated wedges from the bottomside *F* layer, *J. Geophys. Res.*, **87**, 9171, 1982.
- Valladares, C. E., W. B. Hanson, J. P. McClure, and B. L. Cragin, Bottomside sinusoidal irregularities in the equatorial *F* region, *J. Geophys. Res.*, **88**, 8025, 1983.
- van Schooneveld, C. (Ed.), *Image Formation from Coherence Functions in Astronomy*, D. Reidel, Norwell, Mass., 1979.
- Wilczek, R., and S. Drapatz, A high accuracy algorithm for maximum entropy image restoration in the case of small data sets, *Astron. Astrophys.*, **142**, 9, 1985.
- Woodman, R. F., Inclination of the geomagnetic field measured by an incoherent scatter technique, *J. Geophys. Res.*, **76**, 178, 1971.
- Woodman, R. F., and C. La Hoz, Radar observations of *F* region equatorial irregularities, *J. Geophys. Res.*, **81**, 5447, 1976.
- Wu, N., A revised Gull-Daniell algorithm in the maximum entropy method, *Astron. Astrophys.*, **139**, 555, 1984.
- Zargham, S., and C. E. Seyler, Collisional interchange instability, 1, Numerical simulations of intermediate-scale irregularities, *J. Geophys. Res.*, **92**, 10,073, 1987.

D. L. Hysell, Department of Physics and Astronomy, 205 Kinard Laboratory, Clemson University, Clemson, South Carolina 29634. (e-mail: daveh@vlasov.phys.clemson.edu)

(Received January 22, 1996; revised July 29, 1996; accepted July 30, 1996.)